



The Effect of Pinned Photodiode Shape on Time-of-Flight Demodulation Contrast

Terrence Cole Millar, Navid Sarhangnejad, *Student Member, IEEE*, Nikola Katic, *Member, IEEE*, Kyros Kutulakos, and Roman Genov, *Senior Member, IEEE*

Abstract—An empirical investigation on improving the pinned photodiode (PPD) demodulation contrast by tailoring the geometry of the device is presented. Results of this TCAD simulation-based study are used to develop a structure especially suited for time-of-flight applications. In order to obtain a fair comparison between various PPD shapes, a square structure is adopted as a benchmark and all subsequent PPD geometries use the same process parameters. Five different PPD shapes are compared: 1) nominal square-shaped PPD; 2) triangular PPD; 3) constant-field PPD; 4) L-shaped constant-field PPD; and 5) proposed PPD. Device physics simulations are undertaken and the speed of each structure is evaluated on the basis of its demodulation contrast. It is shown that triangular and constant-field PPDs can provide significant improvement compared with a conventional square-shaped PPD, however they still lack effective lateral charge transfer in the final electron sorting stage. The final PPD proposed in this paper achieves this with a tailored PPD shape and doping gradient. In addition, the transfer gates are placed close to one another to make use of gate-induced fringe fields and thus improve the speed of electron sorting. Using these techniques, a PPD demodulation contrast of 61% is obtained at a frequency of 100 MHz, which is comparable to the contrast achieved in state-of-the-art photogate-based designs.

Index Terms—Active pixels, CMOS image sensors, LIDAR, photon-mixing device (PMD), pinned photodiode (PPD), quantum efficiency modulation, time-of-flight (ToF).

I. INTRODUCTION

TIME-OF-FLIGHT (ToF) cameras are emerging as a very promising technology with many potential applications [1], [2]. They provide depth information of the camera's field of view, and can, therefore, give a 3-D representation of a scene without computationally expensive postprocessing. Consequently, over the last several years, they have been extensively studied through rapidly increasing development

Manuscript received January 10, 2017; revised February 14, 2017; accepted February 28, 2017. Date of publication March 15, 2017; date of current version April 19, 2017. This work was supported in part by NSERC under the Strategic Grants and Discovery Grants Program and in part by DARPA under the REVEAL Program. The review of this paper was arranged by Editor C. Surya.

T. C. Millar, N. Sarhangnejad, N. Katic, and R. Genov are with the Department of Electrical and Computer Engineering, University of Toronto, Toronto, ON M5S3G4, Canada (e-mail: colemillar94@gmail.com; sarhangn@ece.utoronto.ca; katic.nik@gmail.com; roman@eecg.utoronto.ca).

K. Kutulakos is with the Department of Computer Science, University of Toronto, Toronto, ON M5S3G4, Canada (e-mail: kyros@cs.toronto.edu).

Color versions of one or more of the figures in this paper are available online at <http://ieeexplore.ieee.org>.

Digital Object Identifier 10.1109/TED.2017.2677201

efforts both in industry and academia. The reason behind such a focused attention is the large number of potential applications: augmented and virtual reality (for gesture and object recognition), advanced driver-assistance systems, self-driving cars, 3-D scanners, video games, biomedical imaging systems, drones, and robots.

An effective way of implementing ToF camera sensors is by using pixels based on single photon avalanche diodes (SPADs) [3]–[9]. SPADs can provide high depth resolution with down to millimeter range accuracy, but require dealing with complex intricacies related to device physics, which increases their development price.

Thanks to their smaller physical size and lower development costs, an attractive alternative to SPADs are ToF pixels based on photon-mixing devices (PMDs). By strictly defining the timing (both phase and frequency) of photodetector charge integration and transfer, these devices can perform demodulation of the light signal emitted from a modulated light source and reflected by the objects in the scene. PMD pixels can determine the phase difference between the transmitted and received light (which translates directly to depth) even in the presence of significant ambient light. One of the pioneering efforts in developing charge coupled devices that can perform photon mixing was described in [10]. This paper was later built on and improved over the years [11]–[14].

In modern implementations, PMDs are typically fabricated using standard CMOS processes. Photogates are commonly used as light detectors due to their inherently high demodulation speed [15]–[17]. On the other hand, photodiodes (PPDs in particular) typically provide higher quantum efficiency, less noise (and, therefore, higher depth resolution), and better spectral response than photogates. However, in their nominal form, photodiodes suffer from a lack of lateral electric field, which results in a slow lateral charge transfer. A combination of photodiodes with gates over the field oxide is used in [18] to exploit the benefits of superior spectral response while still achieving high charge transfer speed. Designs in [19]–[22] use extended gates over the PPDs to generate a lateral electric field and improve the charge transfer speed. A different technique to improve the speed of PPD charge transfer is described in [23] by using very wide (9 μm) charge transfer gates (TGs). The same design was later modified to implement transistor and floating diffusion sharing and to reduce the pixel size [24], [25]. A single-tap (one bucket) structure with concentric gates is developed in [26] to push electrons toward the center of the diode. Sensors in [27]–[29] take the

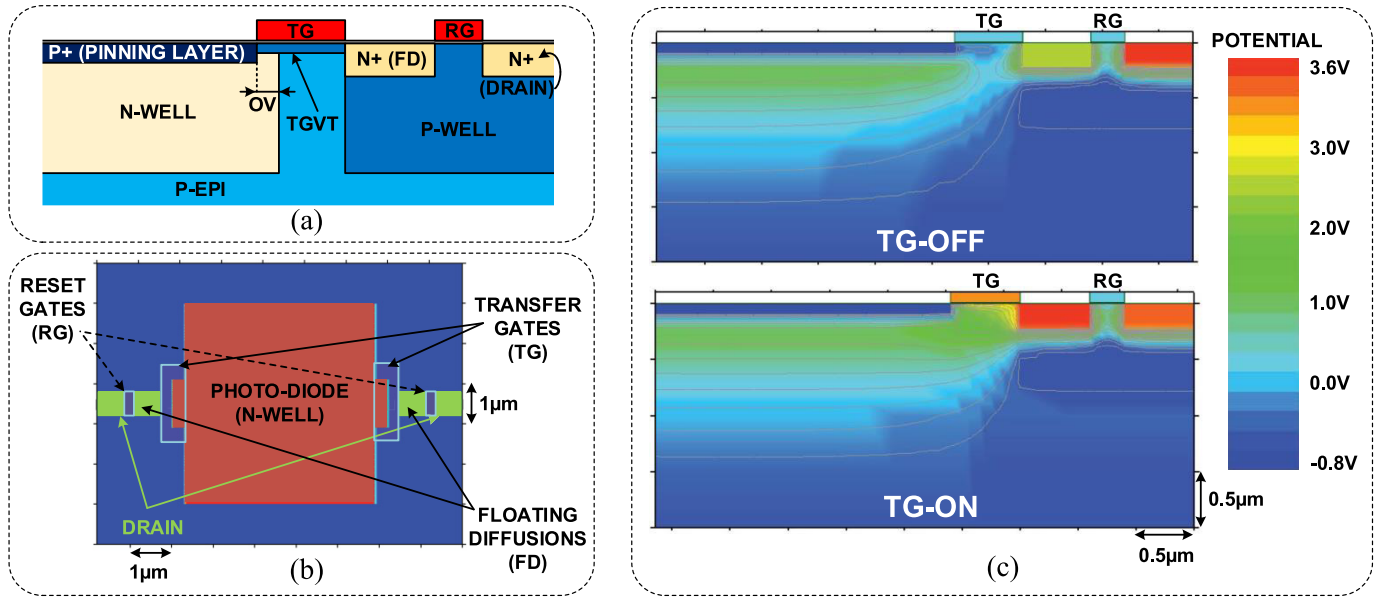


Fig. 1. Benchmark gate design and nominal photodiode structure used for comparison. (a) TG design illustration, including n-well to TG overlap (OV) and TG threshold adjusting (TGVT) layer. (b) Top view of the nominal (square) photodiode structure with two floating diffusions (buckets/taps). Overlap OV of $0.3 \mu\text{m}$ is used in this example for illustration clarity. An overlap of $0.1 \mu\text{m}$ is found to be optimal for the process parameters used in this paper. (c) Potential profile with the TG OFF (top) and ON (bottom) after optimization shows no visible potential pockets or barriers.

gate-induced lateral field technique one step further by performing the photon mixing with lateral electric field modulation using a specially designed set of gates.

Gate-induced lateral field techniques do come with certain drawbacks. If the gates are placed on top of the photosensitive part of the diode (as, for example, in [19]–[21]), the gates reduce the amount of light that reaches the diode by absorbing and reflecting it, therefore causing a reduction in quantum efficiency. If the gates are placed on the side of the photosensitive part of the diode (as, for example, in [27]–[29]), this lowers the pixel fill factor, again reducing the amount of light reaching the photodiode. These tradeoffs have forced researchers to explore alternative ways to create a lateral electric field in a PPD. One of those ways is to induce the lateral field by creating a doping concentration gradient [30]. Another approach is to tailor the potential profile by modifying the photodiode shape as in [31] and [32].

This paper investigates lateral electric field formation by the shape of the PPD. The effect of the photodiode shape is investigated by defining a benchmark, keeping all the parameters constant except for the shape of the photodiode and comparing the following structures in terms of demodulation contrast: 1) nominal square-shaped PPD; 2) triangular PPD; 3) constant-field PPD; 4) L-shaped constant-field PPD; and 5) proposed PPD. Single-tap [22], [23], [26], [32] and two-tap pixel structures [18]–[21], [23], [25], [31] are the most widely used in ToF applications. In terms of photodetecting structure, single-tap structures are very similar to two-tap topologies once the drain/reset gates are added [22], [23], [32]. For this reason, two-tap structures are assumed in this paper. The photodetectors containing four taps [27]–[30] are typically symmetrical devices that can be divided into two pairs of two-tap devices. Therefore, the results of this paper could

(with some caution) be extrapolated to these devices as well. Based on the obtained results, a gradient in doping concentration (a technique previously proposed in [30] and [33]) is combined with the photodiode shape proposed in this paper to achieve a final boost in performance and form an overall effective solution for high charge transfer speed and thus high demodulation contrast.

II. DEMODULATION CONTRAST VERSUS PPD SHAPE

In order to isolate and compare the effect of the PPD shape on lateral charge transfer speed, a clearly defined benchmark is needed. By using a reasonable benchmark, the obtained results could be mapped to different fabrication processes. Even though the actual process tuning will determine the final parameters/performance of the device, some general conclusions related to the performance of different PPD shapes will still hold. Therefore, the same process parameter values are used in all the structures, as well as the same TG design. The metric of comparison is the demodulation contrast, a crucial parameter in ToF applications. Therefore, this section is divided in two parts: 1) benchmark definition and 2) structure performance.

A. Benchmark Definition

All the investigated PPD structures have the same TG structure, as shown in Fig. 1(a). As in conventional image sensors used in high frame rate applications, the goal of the ToF pixel is to make the charge transfer as quick and efficient as possible. The TG threshold voltage adjusting layer [TGVT in Fig. 1(a)] is necessary to ensure a voltage barrier when the TG is OFF [34]. An efficient charge transfer requires losing as few carriers as possible due to charge barriers and/or charge pockets. Adjusting how much the TG overlaps the diode n-well

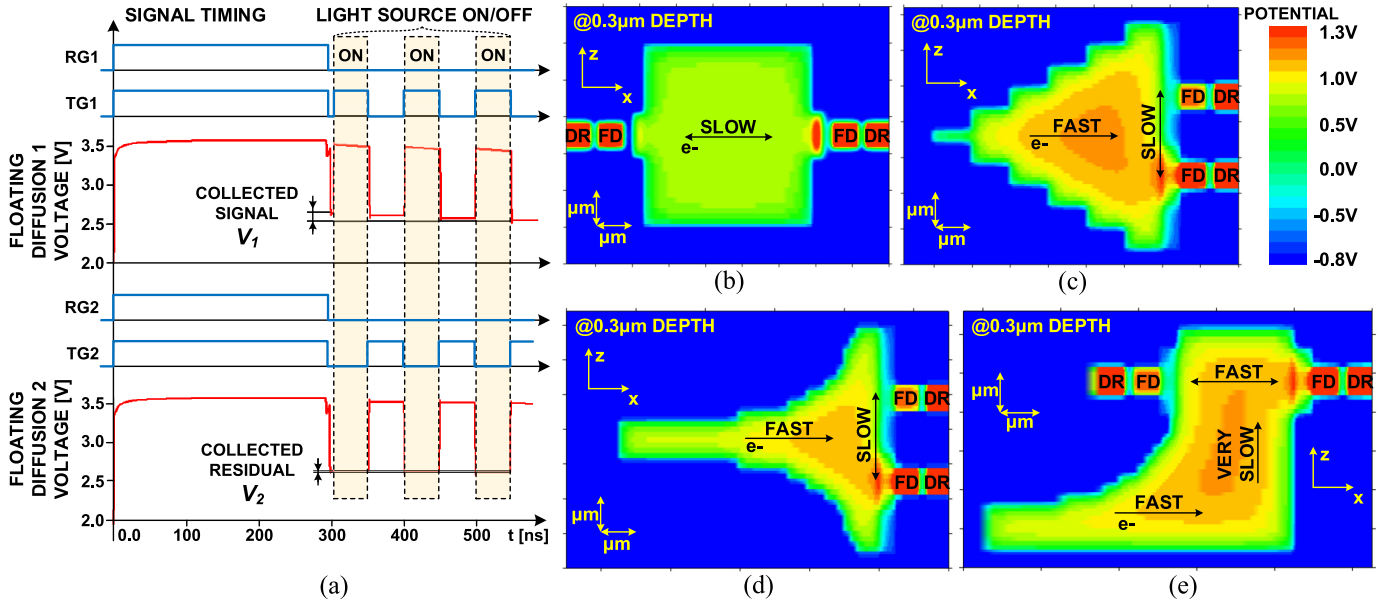


Fig. 2. Signal timing for observing the demodulation contrast and the investigated PPD structures/shapes with the corresponding potential profiles at $0.3 \mu\text{m}$ depth (DR refers to drain diffusion and FD refers to floating diffusion). (a) Typical waveforms of the demodulation contrast simulations. (b) Nominal (square) PPD structure. (c) Triangular structure [32]. (d) Constant-field structure [31]. (e) L-shaped constant-field structure.

helps ensure there are no large pockets or barriers [35] [overlap OV in Fig. 1(a)]. By adjusting the TGVT layer doping, the potential pocket versus potential barrier tradeoff can be fine-tuned to allow for a very efficient charge transfer [35]. The doping concentration of TGVT layer is set to $10^{17}/\text{cm}^3$ in all the following simulations, while the optimal value for the TG/n-well overlap (OV) was found to be $0.1 \mu\text{m}$ (as a comparison, approximately $0.3 \mu\text{m}$ offset/overlap was found to be optimal for a different device structure [35]). The overlap provides a smooth potential profile as seen in Fig. 1(c), with no observable potential pockets or barriers. The TG length and width are the same for all the investigated structures and are 0.6 and $1.8 \mu\text{m}$, respectively.

A conventional square-shaped PPD with two taps and two reset gates RG (one pair on each side) is used as a reference/nominal structure [Fig. 1(a) and (b)]. The doping concentration of the photodiode n-well is set to start at $10^{17}/\text{cm}^3$ close to the surface and gradually decrease to $10^{15}/\text{cm}^3$ at a depth of approximately $0.5 \mu\text{m}$ below the surface [34]. The p+ pinning layer of the PPD is highly doped ($10^{19}/\text{cm}^3$), while the p-substrate is lightly doped to obtain a deep depletion region [$10^{15}/\text{cm}^3$, similar to p-epitaxial layers and the same as in [34]—P-EPI in Fig. 1(a)]. P-well doping concentration is set to $10^{17}/\text{cm}^3$. In all simulations, the structures are exposed to light at a wavelength of 500 nm with an intensity of $100 \text{ W}/\text{m}^2$. The performance of the investigated structures is assessed by comparing the demodulation contrast they achieve, which is covered in Section II-B.

B. Structure Performance

Demodulation contrast is a very important pixel parameter in ToF applications, and a very suitable parameter to compare the performance of the studied PPD shapes. It depends heavily on charge transfer efficiency and speed, and it greatly affects

the final depth resolution of the ToF camera. The standard deviation of the depth measurement error in ToF cameras [12] can be approximately written as

$$\sigma_d = \frac{d}{2\sqrt{2}} \cdot \frac{\sqrt{N_{\text{background}} + N_{\text{noise}} + PE_{\text{opt}}}}{2 \cdot C_{\text{mod}} \cdot C_{\text{demod}} \cdot PE_{\text{opt}}} \quad (1)$$

where d is the maximum measurable depth (nonambiguity distance range), PE_{opt} is the total number of electrons per pixel generated by the modulated light source, $N_{\text{background}}$ is the number of background light electrons, and N_{noise} is the number of electrons corresponding to noise (shot noise, thermal noise, $1/f$ noise, and so on). The modulation contrast C_{mod} defines the effectiveness of light intensity modulation (by the light source), and C_{demod} is the demodulation contrast of the sensor. The depth measurement error is inversely proportional to the demodulation contrast making it a very important pixel parameter in ToF applications. The useful information in ToF cameras is contained only in the light coming from the modulated light source. This signal has to be separated from the background, and, therefore, in the most general form, the demodulation contrast represents the ratio between the useful signal intensity (measured amplitude) and the background intensity (measured offset) [12]. The exact formula for the demodulation contrast, therefore, depends on the shape of the modulation signal and the method used to recover the signal amplitude from the measurement samples. When measured with signal only (no background), the demodulation contrast becomes the ratio of the amplitude and signal dc level (offset) and provides an insight of how efficient the pixel is in quickly and correctly sorting electrons.

For the square-wave signal case, the demodulation contrast can be estimated based on an expression similar to the Michelson contrast formula [36]

$$C_{\text{demod}} = \frac{N_1 - N_2}{N_1 + N_2} \quad (2)$$

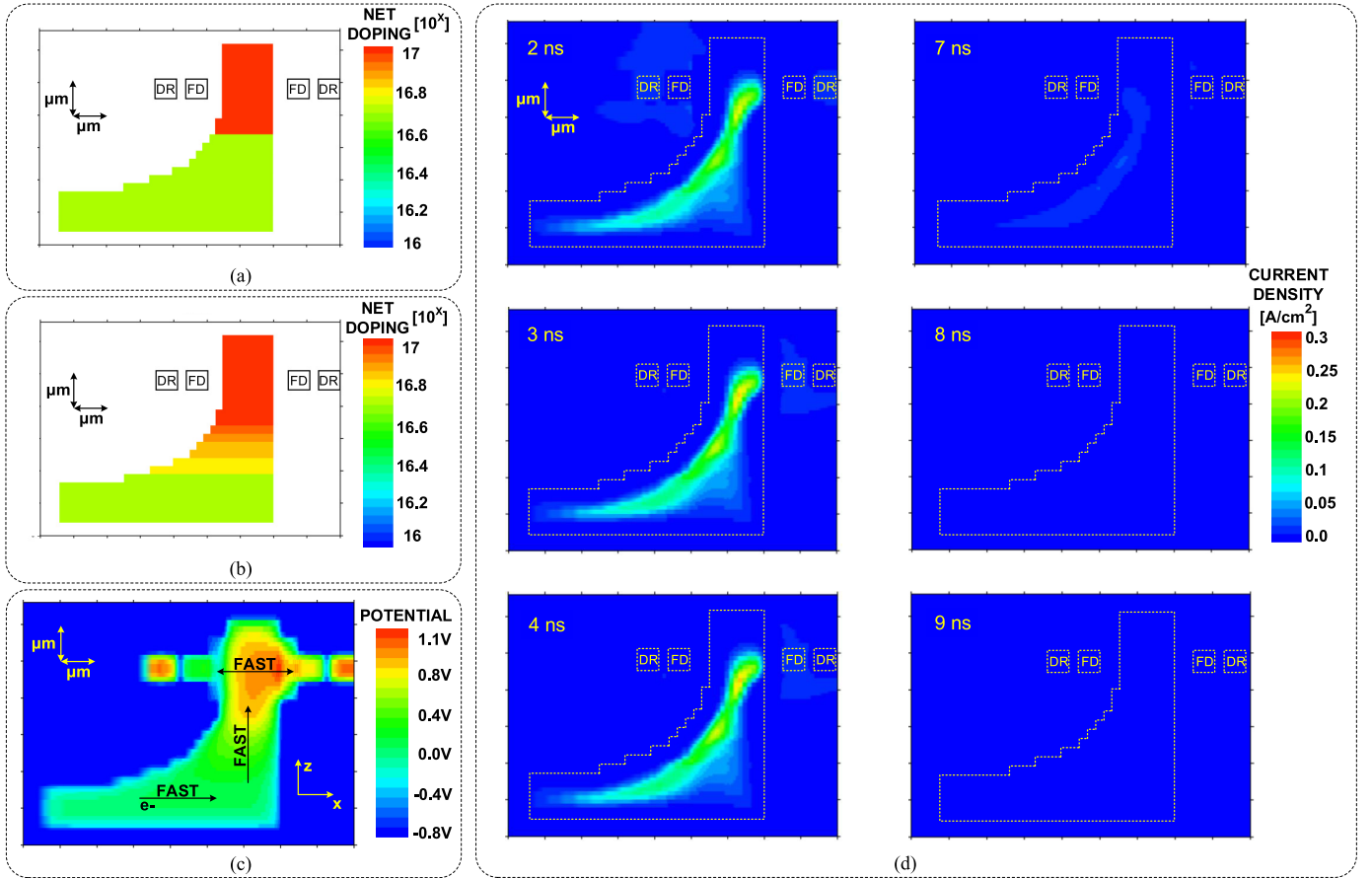


Fig. 3. Proposed structure (DR refers to drain diffusion and FD refers to floating diffusion). (a) With the step doping profile. (b) With the quasi-linear gradient of the doping profile. (c) Potential profile of the quasi-linear gradient structure. (d) Evolution of the current density within the PPD over 10 ns—almost all of the electrons are transferred into the first tap (bucket) during the first 5 ns, and during the last 5 ns, only a negligible current density is observed.

where N_1 and N_2 are the total number of electrons collected by the first and second tap (floating diffusions), respectively, when the received modulated signal and the demodulation signal are perfectly aligned in phase. In the case of an ideal pixel, all the electrons will be collected by the first tap and N_2 will be zero (100% demodulation contrast). If any of the electrons are not transferred to the first tap and get collected by the second tap, then N_2 will be larger than zero resulting in $C_{\text{demod}} < 1$. The corresponding simulation setup and waveforms are shown in Fig. 2(a). Initially, all TG and reset gate are turned ON, therefore resetting both floating diffusions and depleting the PPD. All four signals are then turned OFF in order to obtain the initial voltage level of the FDs. After this initial stage, the modulation starts, and the light is turned ON as a square pulse in perfect phase alignment with turning ON the first TG (signal TG1). After this initial square pulse, the light and TG1 are turned OFF while TG2 is turned ON. TG2 remains ON for the same pulsewidth, and then the cycle repeats. In this way, the first FD collects the signal while the second FD collects the residual. After a reasonable number of modulation signal periods, the demodulation contrast is calculated as in expression (2), using the appropriate voltage differences instead of the raw electron count [see Fig. 2(a)]

$$C_{\text{demod}} = \frac{V_1 - V_2}{V_1 + V_2}. \quad (3)$$

The contrast is simulated at two different frequencies of interest 10 and 100 MHz, which represent the practical modulation range and also the range seen in state-of-the-art ToF cameras. For instance, Microsoft's ToF sensor in [15] is one of the fastest reported demodulating sensors operating at up to 130 MHz, achieving a demodulation contrast of 58% at this frequency.

The investigated PPD shapes with the corresponding potential profiles at 0.3 μm depth are shown in Fig. 2(b)–(e). Due to having practically no lateral field, the square structure in Fig. 2(b) (5 μm × 5 μm) provides a demodulation contrast of 61% at 10 MHz and almost 0% at 100 MHz. The longitudinal electric field introduced by the triangular structure [32] [Fig. 2(c)] improves the demodulation contrast to 85% at 10 MHz and 12% at 100 MHz. Additional improvement is observed in a constant-field structure [31] [Fig. 2(d)], which provides a demodulation contrast of 89% at 10 MHz and 15% at 100 MHz. Even though a constant-field structure [Fig. 2(d)] offers certain improvement over the triangular structure [Fig. 2(c)], getting good contrast at high frequencies clearly requires more than simply changing the side-edge shape of the PPD. One obvious drawback of these two structures is that the PPD is widest at the point where the floating diffusions are located. Therefore, once the signal charge is transferred to the wide part of the diode

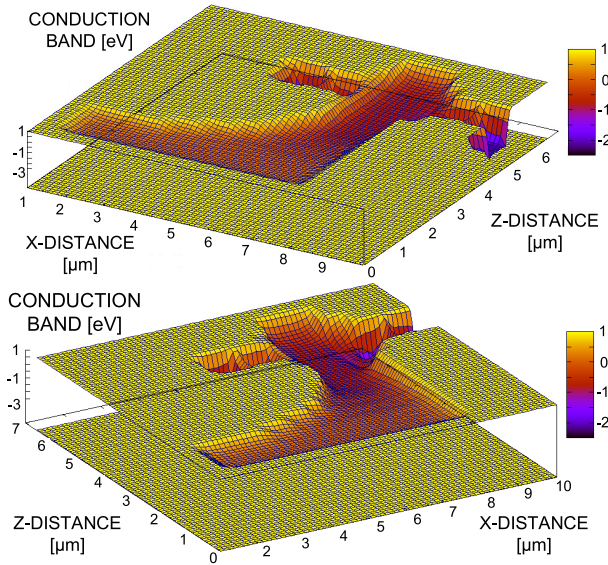


Fig. 4. 3-D graph of the potential profile for the final proposed structure shown from two different angles. The effect of the lateral electric fields can be observed, making a smooth fall in the potential profile toward the mixing (electron sorting) region.

by the shape-induced electric field, it still needs to travel from one side of the diode to the other [z -direction in Fig. 2(c) and (d)], making the corresponding transfer and final sorting of electrons slow. In order to improve the final sorting of electrons, a modified structure is investigated [Fig. 2(e)], in which the constant-field structure is shaped such that the taps and TGs can be placed more closely together. This allows the fringing electric fields from the TGs to be more effective in final electron sorting. However, this particular structure provides a demodulation contrast of only 74% at 10 MHz and effectively 0% at 100 MHz. The drawback of this structure is that, because the diode gets narrower in the z -direction [Fig. 2(e)], there is a barrier for electrons to travel toward the TGs, which severely affects the final performance. The general differences in electron transfer speed between the structures are roughly illustrated in Fig. 2(b)–(e).

III. PROPOSED STRUCTURE

The study from Section II provided useful insight about both the advantages and disadvantages of the investigated structures. Even though the L-shaped constant-field structure is better at final electron sorting than the previous devices, an additional electric field is needed in order to properly transfer the electrons toward the collection area [in the z -direction in Fig. 2(e)]. This can be done by introducing a doping gradient to the PPD in addition to tailoring the photodiode shape. Two different approaches of adding a doping gradient are investigated in this paper. In version one, the doping gradient is added simply as an abrupt step function [Fig. 3(a)]. Having only two different doping concentrations allows for a relatively simple device fabrication. A doping concentration (at the surface) of $5 \cdot 10^{16}/\text{cm}^3$ is used in the n -well and it steps up to $10^{17}/\text{cm}^3$ close to the TGs. In addition to that, the distance between the TGs is further reduced compared with the

TABLE I
RESULTS SUMMARY

| Structure | Demodulation Contrast @10MHz | Demodulation Contrast @100MHz |
|---------------------------------------|------------------------------|-------------------------------|
| Nominal (square-shape) structure | 61% | 0% |
| Triangular structure | 85% | 12% |
| Constant-field structure | 89% | 15% |
| L-shaped constant-field structure | 74% | 0% |
| Proposed structure v1 (step doping) | 94% | 34% |
| Proposed structure v2 (linear doping) | 96% | 61% |

previously investigated L-shaped structure. This enhances the fringe electric fields in this region, therefore improving the efficiency of the final electron sorting stage. Consequently, the desired lateral field is present everywhere throughout the structure as roughly illustrated in Fig. 3(c). The corresponding structure provides a demodulation contrast of 94% at 10 MHz and 34% at 100 MHz, which is significantly better than any of the previously investigated structures.

The second method for adding the desired electric field is to apply a quasi-linear doping gradient to the same structure [Fig. 3(b)]. The quasi-linear doping gradient is added such that it starts at $5 \cdot 10^{16}/\text{cm}^3$ on the bottom side of the diode [see Fig. 3(b)] and then increases gradually until $10^{17}/\text{cm}^3$ at the TGs. The potential profile for this structure is shown in Fig. 3(c). The structure provides a demodulation contrast of 96% at 10 MHz and 61% at 100 MHz. The charge transfer speed of the final structure using the linear doping gradient is illustrated in Fig. 3(d), which represents the current density in the PPD during one demodulation period of 10 ns (100 MHz). During the first 5 ns, a significant current density is observed and the electrons are effectively conveyed toward the first tap (bucket). During the second (residual) phase, significantly lower current density is observed, which corresponds to and illustrates the reduced portion of electrons contributing to an error signal. Fig. 4 shows a 3-D version of the potential profile for the final structure with the linear doping gradient. It can be seen that the electric fields are designed such that they convey electrons toward the collection area (TGs) from any point within the PPD.

IV. CONCLUSION

The summary of the final results is given in Table I. For large PPD sizes, the lateral field induced by the TGs is not enough to effectively move electrons from the middle of the diode, resulting in poor performance of square structures especially at high frequency. Triangular and constant-field structures provide significant improvement compared with conventional square-shaped PPDs, however they still struggle in the final electron sorting stage. In order to achieve high charge transfer speed, an effective lateral electric field is needed in every section of the PPD such that electrons can both be conveyed toward the collection area (close to the TGs), and then also be sorted effectively by the TGs. This is achieved by the structure proposed in this paper [Figs. 3(b) and (c) and 4], by combined tailoring of the PPD shape and doping gradient. Using this simple technique, a demodulation contrast of 61% is achieved at a frequency of 100 MHz, which is

comparable to the contrast achieved in state-of-the-art photogate-based designs, such as Microsoft's ToF sensor in [15] (58% demodulation contrast at 130 MHz). The proposed technique can also be extended to a symmetric version of the same shape (for use in fully differential pixels) or to pixels that implement four taps for better performance in motion intensive environments. The possibility of having robust multitap demodulation pixels with performance comparable to photogates, but with the superior noise characteristics of PPDs, is worth pursuing if the challenges of fabricating the device can be met and overcome.

REFERENCES

- [1] M. Hansard, S. Lee, O. Choi, and R. P. Horaud, *Time-of-Flight Cameras: Principles, Methods and Applications*. London, U.K.: Springer, 2012.
- [2] S. Foix, G. Alenya, and C. Torras, "Lock-in time-of-flight (ToF) cameras: A survey," *IEEE Sensors J.*, vol. 11, no. 9, pp. 1917–1926, Sep. 2011.
- [3] C. Niclass, A. Rochas, P.-A. Besse, and E. Charbon, "Design and characterization of a CMOS 3-D image sensor based on single photon avalanche diodes," *IEEE J. Solid-State Circuits*, vol. 40, no. 9, pp. 1847–1854, Sep. 2005.
- [4] D. Stoppa, L. Pancheri, M. Scandiuozzo, L. Gonzo, G.-F. Dalla Betta, and A. Simoni, "A CMOS 3-D imager based on single photon avalanche diode," *IEEE Trans. Circuits Syst. I, Reg. Papers*, vol. 54, no. 1, pp. 4–12, Jan. 2007.
- [5] O. Shcherbakova, L. Pancheri, G.-F. Dalla Betta, N. Massari, and D. Stoppa, "3D camera based on linear-mode gain-modulated avalanche photodiodes," in *IEEE Int. Solid-State Circuits Conf. Dig. Tech. Papers*, Apr. 2013, pp. 490–491.
- [6] R. J. Walker, J. A. Richardson, and R. K. Henderson, "A 128×96 pixel event-driven phase-domain $\Delta\Sigma$ -based fully digital 3D camera in 0.13 μm CMOS imaging technology," in *Proc. IEEE Int. Solid-State Circuits Conf.*, Apr. 2011, pp. 410–412.
- [7] C. Niclass, M. Soga, H. Matsubara, S. Kato, and M. Kagami, "A 100-m range 10-frame/s 340×96-pixel time-of-flight depth sensor in 0.18- μm CMOS," *IEEE J. Solid-State Circuits*, vol. 48, no. 2, pp. 559–572, Feb. 2013.
- [8] C. Niclass, M. Soga, H. Matsubara, M. Ogawa, and M. Kagami, "A 0.18- μm CMOS SoC for a 100-m-range 10-frame/s 200×96-pixel time-of-flight depth sensor," *IEEE J. Solid-State Circuits*, vol. 49, no. 1, pp. 315–330, Jan. 2014.
- [9] M. Perenzoni, D. Perenzoni, and D. Stoppa, "A 64×64-pixel digital silicon photomultiplier direct ToF sensor with 100Mphotons/s/pixel background rejection and imaging/altimeter mode with 0.14% precision up to 6km for spacecraft navigation and landing," in *Proc. IEEE Int. Solid-State Circuits Conf. (ISSCC)*, Apr. 2016, pp. 118–119.
- [10] T. Spirig, P. Seitz, O. Vietze, and F. Heitger, "The lock-in CCD-two-dimensional synchronous detection of light," *IEEE J. Quantum Electron.*, vol. 31, no. 9, pp. 1705–1708, Sep. 1995.
- [11] R. Lange, P. Seitz, A. Biber, and S. C. Lauxtermann, "Demodulation pixels in CCD and CMOS technologies for time-of-flight ranging," *Proc. SPIE*, vol. 3965, pp. 177–188, May 2000.
- [12] R. Lange and P. Seitz, "Solid-state time-of-flight range camera," *IEEE J. Quantum Electron.*, vol. 37, no. 3, pp. 390–397, Mar. 2001.
- [13] B. Buttgen, F. Lustenberger, and P. Seitz, "Demodulation pixel based on static drift fields," *IEEE Trans. Electron Devices*, vol. 53, no. 11, pp. 2741–2747, Nov. 2006.
- [14] B. Buttgen and P. Seitz, "Robust optical time-of-flight range imaging based on smart pixel structures," *IEEE Trans. Circuits Syst. I, Reg. Papers*, vol. 55, no. 6, pp. 1512–1525, Jun. 2008.
- [15] C. S. Bamji *et al.*, "A 0.13 μm CMOS system-on-chip for a 512 × 424 time-of-flight image sensor with multi-frequency photo-demodulation up to 130 MHz and 2 GS/s ADC," *IEEE J. Solid-State Circuits*, vol. 50, no. 1, pp. 303–319, Jan. 2015.
- [16] A. Payne *et al.*, "A 512×424 CMOS 3D time-of-flight image sensor with multi-frequency photo-demodulation up to 130 MHz and 2GS/s ADC," in *IEEE Int. Solid-State Circuits Conf. (ISSCC) Dig. Tech. Papers*, Sep. 2014, pp. 134–135.
- [17] S. B. Gokturk, H. Yalcin, and C. Bamji, "A time-of-flight depth sensor-system description, issues and solutions," in *Proc. Conf. Comput. Vis. Pattern Recognit. Workshop, (CVPRW)*, 2004, pp. 1–35.
- [18] S. Kawahito, I. A. Halin, T. Ushinaga, T. Sawada, M. Homma, and Y. Maeda, "A CMOS time-of-flight range image sensor with gates-on-field-oxide structure," *IEEE Sensors J.*, vol. 7, no. 12, pp. 1578–1586, Dec. 2007.
- [19] D. Stoppa, N. Massari, L. Pancheri, M. Malfatti, M. Perenzoni, and L. Gonzo, "An 80×60 range image sensor based on 10 μm 50 MHz lock-in pixels in 0.18 μm CMOS," in *IEEE Int. Solid-State Circuits Conf. (ISSCC) Dig. Tech. Papers*, Sep. 2010, pp. 406–407.
- [20] D. Stoppa, N. Massari, L. Pancheri, M. Malfatti, M. Perenzoni, and L. Gonzo, "A range image sensor based on 10- μm lock-in pixels in 0.18 μm CMOS imaging technology," *IEEE J. Solid-State Circuits*, vol. 46, no. 1, pp. 248–258, Jan. 2011.
- [21] L. Pancheri, N. Massari, M. Perenzoni, M. Malfatti, and D. Stoppa, "A QVGA-range image sensor based on buried-channel demodulator pixels in 0.18 μm CMOS with extended dynamic range," in *Proc. IEEE Int. Solid-State Circuits Conf.*, Apr. 2012, pp. 394–396.
- [22] W. Kim *et al.*, "A 1.5 Mpixel RGBZ CMOS image sensor for simultaneous color and range image capture," in *Proc. IEEE Int. Solid-State Circuits Conf.*, Sep. 2012, pp. 392–394.
- [23] S.-J. Kim, S.-W. Han, B. Kang, K. Lee, J. D. Kim, and C.-Y. Kim, "A three-dimensional time-of-flight CMOS image sensor with pinned-photodiode pixel structure," *IEEE Electron Device Lett.*, vol. 31, no. 11, pp. 1272–1274, Nov. 2010.
- [24] S.-J. Kim, J. D. Kim, S.-W. Han, B. Kang, K. Lee, and C.-Y. Kim, "A 1920×480 image sensor with unified pixel architecture for 2D/3D imaging in 0.11 μm CMOS," in *Proc. VLSI Circuits (VLSIC) Symp.*, 2011, pp. 92–93.
- [25] S.-J. Kim, B. Kang, J. D. Kim, K. Lee, C.-Y. Kim, and K. Kim, "A 1920×1080 3.65 μm -pixel 2D/3D image sensor with split and binning pixel structure in 0.11 μm standard CMOS," in *Proc. IEEE Int. Solid-State Circuits Conf.*, Jun. 2012, pp. 396–398.
- [26] T.-Y. Lee *et al.*, "A time-of-flight 3-D image sensor with concentric-photogates demodulation pixels," *IEEE Trans. Electron Devices*, vol. 61, no. 3, pp. 870–877, Mar. 2014.
- [27] S. M. Han, T. Takasawa, K. Yasutomi, S. Aoyama, K. Kagawa, and S. Kawahito, "A time-of-flight range image sensor with background canceling lock-in pixels based on lateral electric field charge modulation," *IEEE J. Electron Devices Soc.*, vol. 3, no. 3, pp. 267–275, May 2015.
- [28] S.-M. Han, T. Takasawa, T. Akahori, K. Yasutomi, K. Kagawa, and S. Kawahito, "A 413×240-pixel sub-centimeter resolution time-of-flight CMOS image sensor with in-pixel background canceling using lateral-electric-field charge modulators," in *IEEE Int. Solid-State Circuits Conf. (ISSCC) Dig. Tech. Papers*, Apr. 2014, pp. 130–131.
- [29] T. Kasugai *et al.*, "A time-of-flight CMOS range image sensor using 4-tap output pixels with lateral-electric-field control," *Electron. Imag.*, vol. 2016, no. 12, pp. 1–6, 2016.
- [30] A. Spickermann *et al.*, "CMOS 3D image sensor based on pulse modulated time-of-flight principle and intrinsic lateral drift-field photodiode pixels," in *Proc. ESSCIRC*, 2011, pp. 111–114.
- [31] H. Takeshita, T. Sawada, T. Iida, K. Yasutomi, and S. Kawahito, "High-speed charge transfer pinned-photodiode for a CMOS time-of-flight range image sensor," *Proc. SPIE*, vol. 7536, pp. 75360R–75360R, Jan. 2010.
- [32] C. Tubert, L. Simony, F. Roy, A. Tourmier, L. Pinzelli, and P. Magnan, "High speed dual port pinned-photodiode for time-of-flight imaging," in *Proc. IISW*, 2009, pp. 1–3.
- [33] D. Durini *et al.*, "Lateral drift-field photodiode for low noise, high-speed, large photoactive-area CMOS imaging applications," *Nucl. Instrum. Methods Phys. Res. Sec. A, Accel., Spectrometers, Detectors Associated Equip.*, vol. 624, no. 2, pp. 470–475, 2010.
- [34] E. R. Fossum and D. B. Hondongwa, "A review of the pinned photodiode for CCD and CMOS image sensors," *IEEE J. Electron Devices Soc.*, vol. 2, no. 3, pp. 33–43, May 2014.
- [35] Y. Zhou, Z. Cao, Q. Li, Q. Qin, and N. Wu, "Image lag optimization of four-transistor pixel for high speed CMOS image," *Proc. SPIE*, vol. 8194, pp. 819435, Aug. 2011.
- [36] *Introduction to the Time-of-Flight (ToF) System Design*, Texas Instruments, Dallas, TX, USA, 2014.



Terrence Cole Millar received the B.Sc. degree in engineering physics from the University of Toronto, Toronto, ON, Canada, in 2016. He was a Student Researcher with the Intelligent Sensory Microsystems Laboratory, University of Toronto, from 2015 to 2016. His current research interests include the physics of semiconductor devices and designing optical devices.



Kyros Kutulakos received the B.S. degree in computer science from the University of Crete, Rethymno, Greece, in 1988, and the Ph.D. degree in computer science from the University of Wisconsin–Madison, Madison, WI, USA, in 1994. He is currently a Professor of Computer Science with the University of Toronto, Toronto, ON, Canada.



Navid Sarhangnejad (S'15) received the B.Sc. degree from the University of Tehran, Tehran, Iran, in 2008, and the M.S. degree in electrical and computer engineering from the Delft University of Technology, Delft, The Netherlands, in 2010. After working for CMOSIS for several years, he is currently pursuing the Ph.D. degree in electrical and computer engineering with the University of Toronto, Toronto, ON, Canada.



Nikola Katic (S'10–M'14) received the M.Sc. and Ph.D. degrees in electrical and electronic engineering from the Swiss Federal Institute of Technology Lausanne, Lausanne, Switzerland, in 2010 and 2014, respectively. After working for Samsung Electronics, he joined the Department of Electrical and Computer Engineering, University of Toronto, Toronto, ON, Canada, in 2016, as a Post-Doctoral Fellow.



Roman Genov (S'96–M'02–SM'11) received the B.S. degree in electrical engineering from the Rochester Institute of Technology, Rochester, NY, USA, in 1996, and the M.S.E. and Ph.D. degrees in electrical and computer engineering from Johns Hopkins University, Baltimore, MD, USA, in 1998 and 2003, respectively. He is currently a Professor with the University of Toronto, Toronto, ON, Canada.